

Swarthmore College

Works

Physics & Astronomy Faculty Works

Physics & Astronomy

3-1-2023

TESS Discovery Of Twin Planets Near 2:1 Resonance Around Early M Dwarf TOI 4342

E. Tey

C. X. Huang

M. Kunimoto

See next page for additional authors

Follow this and additional works at: <https://works.swarthmore.edu/fac-physics>



Part of the [Astrophysics and Astronomy Commons](#)

[Let us know how access to these works benefits you](#)

Recommended Citation

E. Tey et al. (2023). "TESS Discovery Of Twin Planets Near 2:1 Resonance Around Early M Dwarf TOI 4342". *The Astronomical Journal*. Volume 165, Issue 3. DOI: 10.3847/1538-3881/acaf88
<https://works.swarthmore.edu/fac-physics/477>



This work is licensed under a [Creative Commons Attribution 4.0 International License](#).

This work is brought to you for free by Swarthmore College Libraries' Works. It has been accepted for inclusion in Physics & Astronomy Faculty Works by an authorized administrator of Works. For more information, please contact myworks@swarthmore.edu.

Authors

E. Tey, C. X. Huang, M. Kunimoto, A. Vanderburg, A. Shporer, S. N. Quinn, G. Zhou, K. A. Collins, K. I. Collins, Eric L.N. Jensen, R. P. Schwarz, R. Sefako, T. Gan, E. Furlan, C. L. Gnilka, S. B. Howell, K. V. Lester, C. Ziegler, C. Briceño, N. Law, A. W. Mann, G. R. Ricker, R. K. Vanderspek, D. W. Latham, S. Seager, J. M. Jenkins, J. N. Winn, D. A. Caldwell, D. Charbonneau, C. J. Burke, and Z. Essack



TESS Discovery of Twin Planets near 2:1 Resonance around Early M Dwarf TOI 4342

Evan Tey¹, Chelsea X. Huang², Michelle Kunimoto¹, Andrew Vanderburg¹, Avi Shporer¹, Samuel N. Quinn³, George Zhou², Karen A. Collins³, Kevin I. Collins⁴, Eric L. N. Jensen⁵, Richard P. Schwarz³, Ramotholo Sefako⁶, Tianjun Gan⁷, Elise Furlan⁸, Crystal L. Gnlika⁹, Steve B. Howell⁹, Kathryn V. Lester⁹, Carl Ziegler¹⁰, César Briceño¹¹, Nicholas Law¹², Andrew W. Mann¹², George R. Ricker¹, Roland K. Vanderspek¹, David W. Latham³, S. Seager^{1,13,14}, Jon M. Jenkins⁹, Joshua N. Winn¹⁵, Douglas A. Caldwell^{9,16}, David Charbonneau³, Christopher J. Burke¹, and Zahra Essack^{1,13}

¹ Department of Physics and Kavli Institute for Astrophysics and Space Science, Massachusetts Institute of Technology, 77 Massachusetts Avenue, Cambridge, MA 02139, USA; tey@mit.edu

² University of Southern Queensland, West St, Darling Heights, Toowoomba, Queensland, 4350, Australia

³ Center for Astrophysics | Harvard & Smithsonian, 60 Garden Street, Cambridge, MA 02138, USA

⁴ George Mason University, 4400 University Drive, Fairfax, VA 22030, USA

⁵ Department of Physics and Astronomy, Swarthmore College, 500 College Avenue, Swarthmore, PA 19081, USA

⁶ South African Astronomical Observatory, P.O. Box 9, Observatory, Cape Town, 7935, South Africa

⁷ Department of Astronomy and Tsinghua Centre for Astrophysics, Tsinghua University, Beijing, 100084, People's Republic of China

⁸ Caltech/IPAC-NExScI, NASA Exoplanet Science Institute, 1200 East California Boulevard, Mail Code 100-22, Pasadena, CA 91125, USA

⁹ NASA Ames Research Center, Moffett Field, CA 94035, USA

¹⁰ Department of Physics, Engineering and Astronomy, Stephen F. Austin State University, 1936 North Street, Nacogdoches, TX 75962, USA

¹¹ Cerro-Tololo Inter-American Observatory, Casilla 603, La Serena, Chile

¹² Department of Physics and Astronomy, The University of North Carolina at Chapel Hill, Chapel Hill, NC 27599-3255, USA

¹³ Department of Earth, Atmospheric and Planetary Sciences, Massachusetts Institute of Technology, 77 Massachusetts Avenue, Cambridge, MA 02139, USA

¹⁴ Department of Aeronautics and Astronautics, Massachusetts Institute of Technology, 77 Massachusetts Avenue, Cambridge, MA 02139, USA

¹⁵ Department of Astrophysical Sciences, Princeton University, 4 Ivy Lane, Princeton, NJ 08544, USA

¹⁶ SETI Institute, Moffett Field, Mountain View, CA 94035, USA

Received 2022 October 19; revised 2022 December 21; accepted 2022 December 29; published 2023 February 9

Abstract

With data from the Transiting Exoplanet Survey Satellite (TESS), we showcase improvements to the MIT Quick Look Pipeline (QLP) through the discovery and validation of a multiplanet system around M dwarf TOI 4342 ($T_{\text{mag}} = 11.032$, $M_{\star} = 0.63 M_{\odot}$, $R_{\star} = 0.60 R_{\odot}$, $T_{\text{eff}} = 3900$ K, $d = 61.54$ pc). With updates to QLP, including a new multiplanet search, as well as faster cadence data from TESS's First Extended Mission, we discovered two sub-Neptunes ($R_b = 2.266_{-0.038}^{+0.038} R_{\oplus}$ and $R_c = 2.415_{-0.040}^{+0.043} R_{\oplus}$; $P_b = 5.538$ days and $P_c = 10.689$ days) and validated them with ground-based photometry, spectra, and speckle imaging. Both planets notably have high transmission spectroscopy metrics of 36 and 32, making TOI 4342 one of the best systems for comparative atmospheric studies. This system demonstrates how improvements to QLP, along with faster cadence full-frame images, can lead to the discovery of new multiplanet systems.

Unified Astronomy Thesaurus concepts: Exoplanet astronomy (486); Transit photometry (1709); M dwarf stars (982)

1. Introduction

The Transiting Exoplanet Survey Satellite (TESS, Ricker et al. 2015) launched on 2018 April 18 with a goal of discovering transiting exoplanets around bright stars across the entire sky. During every sector (~ 27 days), TESS observes a $24^{\circ} \times 96^{\circ}$ swath of the sky during two elongated orbits around the Earth before shifting to the next sector. During its Primary Mission (2018 July 25–2020 July 4), TESS collected photometry at a 2 minutes cadence for $\sim 20,000$ targets in each sector preselected from the Candidate Target List (CTL, Stassun et al. 2018), while full-frame images (FFIs) were collected at a 30 minutes cadence. In these 26 sectors, TESS covered 70% of the sky and found 2241 transiting planet candidates (Guerrero et al. 2021).

The MIT Quick Look Pipeline (QLP, Huang et al. 2020a) has been an important contributor to detecting these planet

candidates, expanding the search from the $\sim 200,000$ CTL stars to millions of stars brighter than $T_{\text{mag}} = 10.5$ in the FFIs. In every sector, QLP searches for planet candidates around stars with $T_{\text{mag}} < 10.5$, making full use of all past sectors of data. Notably, ~ 1000 candidates from the Primary Mission were found around stars *not* on the CTL—a majority of which were detected by QLP.

With its First Extended Mission (2020 July 4–2022 September 1), TESS, and QLP in particular, was well positioned to yield even more candidates, especially as the FFI recording cadence was reduced from 30 minutes to 10 minutes. On 2022 September 1, TESS will have started its Second Extended Mission, and the FFI recording cadence will be reduced further to 200 s. These reductions allow the flux-time series from the FFIs to better resolve transit ingresses and egresses and therefore improve planet detection efficiency. QLP, however, still has room for improvement. We are introducing here three major changes to the pipeline:

1. *Systematic multiplanet search.* In the Primary Mission, QLP only sent the most promising transit candidate from each light curve through future stages of vetting.



Original content from this work may be used under the terms of the [Creative Commons Attribution 4.0 licence](https://creativecommons.org/licenses/by/4.0/). Any further distribution of this work must maintain attribution to the author(s) and the title of the work, journal citation and DOI.

Additional candidates could be reported if the TOI vetters noticed them during visual inspection of the light curves, but no explicit search was otherwise done for these additional planets. Based on our knowledge of close-in exoplanet systems from the Kepler mission, a majority of the small planets reside in multiple planetary systems (Winn & Fabrycky 2015). Adding an automatic search for multiple transit signals will potentially introduce new interesting systems for follow-up studies and allow future statistical studies of system architecture.

2. *Improved difference images.* Difference images (Bryson et al. 2013) are an effective method of determining the source location of a transit signal in the sky. For the Primary Mission, QLP used a simplistic algorithm for creating difference images by directly subtracting the median stacked frames in the in-transit and out-of-transit time windows. By more intelligently selecting frames to avoid systematics, transit ingress/egress, and additional planets in the system, we improve the robustness of the difference images. This reduces QLP’s false positive rate and allows us to reduce human-review times or alternatively expand our search to more stars.
3. *Quaternion detrending.* Previously, QLP detrended light curves by fitting and removing basis splines to correct for long-timescale systematics (Vanderburg & Johnson 2014). However, there are residual systematics on shorter timescales due to spacecraft jitter motions that can have significant effects on light curves, especially for bright stars (Vanderburg et al. 2019; Huang et al. 2020b). We can measure and correct for this jitter with TESS quaternion data—3-vector time series data describing spacecraft attitude every two seconds.¹⁷ For transit signals with relatively small depth and short duration, correcting these systematics is important to improving QLP’s detection sensitivity.

Altogether, these improvements to QLP—along with extended light curves at faster cadence—will increase the scientific output of TESS as a whole. One population that will especially benefit from this are multiplanet systems around M dwarfs. M dwarfs are known to frequently host multiplanetary systems (Dressing & Charbonneau 2015; Ballard 2019). The duration of planetary transits around M dwarfs is often relatively short, making these transits easily diluted in the 30 minute cadence TESS FFI light curves from the Primary Mission. M dwarfs are also the most abundant type of star in our Galaxy. So, even though many have been selected for 2 minutes cadence target pixel stamp observations, plenty are only monitored by the FFIs. The regular multisector processing approach of the QLP also enables us to take the most advantage of all the available data. Finally, M dwarfs are also ideal host stars for atmospheric characterization of their transiting planets. Determining atmospheric composition, especially for multiple planets in a single system, allows us to compare formation and evolutionary histories.

As of 2022 July, TESS has detected 373 candidate transiting planetary systems around nearby M dwarfs.¹⁸ Thirty-six of these systems host multiple planets, including TOI 270

(Gunther et al. 2019; Van Eylen et al. 2021), TOI 175 (Cloutier et al. 2019; Kostov et al. 2019), and TOI 700 (Gilbert et al. 2020; Rodriguez et al. 2020). Building on the original Kepler mission (Kepler Mission 2019), this doubles the number of discovered transiting M-dwarf multiplanet systems.

The discovery of TOI 4342, an M-dwarf system with two transiting sub-Neptunes, showcases the power of the Extended Mission FFIs with the newly added improvements to QLP for detecting multiplanet M-dwarf systems. With the longer baseline, we have more opportunities to catch transits and, together with the faster cadence, we have better statistics to detect the shorter-duration transits that come with M-dwarf systems. Adding short-timescale systematic corrections adds to this sensitivity, and the multiplanet search is what allows us to discover this multiplanet system where the previous version of QLP could not make this discovery.

TOI 4342 (TESS Input Catalog (TIC) 354944123; $T_{\text{mag}} = 11.032$; $d = 61.54$ pc) is an M0V-type star with two transiting sub-Neptunes TOI 4342 b ($2.27 R_{\oplus}$) and TOI 4342 c ($2.41 R_{\oplus}$). The planets are near a 2:1 mean-motion resonance with periods of 5.538 and 10.689 days. Both planets are good targets for atmospheric characterization and comparison studies with transmission spectroscopy metrics ≥ 30 (Kempton et al. 2018).

Both planets were detected with TESS and followed up with ground-based photometry, reconnaissance spectroscopy, and high-resolution imaging. In Section 2 we describe these observations. In Section 3 we perform fits and validate both signals as planetary transits around an M0V host star. In Section 4 we re-emphasize the improvements to QLP and describe the TOI 4342 system in the context of small planets, multiplanet systems, and planets orbiting M dwarfs.

2. Observations and Data Analysis

2.1. TESS

TOI 4342 was first observed by TESS in Sector 13 (Primary Mission, 2019 June 19–July 18) then observed again in Sector 27 (First Extended Mission, 2020 July 4–30) as a 2 minutes target due to its brightness and small radius (Stassun et al. 2019), as well as in FFIs.

The 2 minutes data were reduced by the Science Processing Operations Center (SPOC) pipeline at NASA (Jenkins et al. 2016). The planets’ transit signals were detected during a SPOC multisector search of Sectors 13 and 27 on 2021 May 26 with an adaptive, noise-compensating matched filter (Jenkins 2002; Jenkins et al. 2010, 2017). In the multisector search, the 5 days signal was detected with signal-to-noise ratio (S/N) 10.8 and multiple event statistic (MES) of 8.5, and the 10 days signal was detected with S/N 9.0 and MES 8.2. Both transit signatures passed all the diagnostic tests reported in the SPOC data validation reports (Twicken et al. 2018; Li et al. 2019), including the difference image centroid tests, which located the source of the transits to within $8''7 \pm 5''5$ and $3''4 \pm 3''6$ of the target star image for TOI 4342 b and c, respectively. Both candidates were classified as high-quality candidates by the TESS-ExoClass classifier.¹⁹ TESS-ExoClass applies a series of tests based on the Kepler Robovetter (Coughlin et al. 2016; Thompson et al. 2018) to pass the best candidates on to the manual TOI vetting process (Guerrero et al. 2021). These exoplanet signatures were

¹⁷ Quaternion data are available online at <https://archive.stsci.edu/missions/teess/engineering/>

¹⁸ The TESS candidate list was downloaded from the NASA Exoplanet Archive on 2022 July 7.

¹⁹ <https://github.com/christopherburke/TESS-ExoClass>

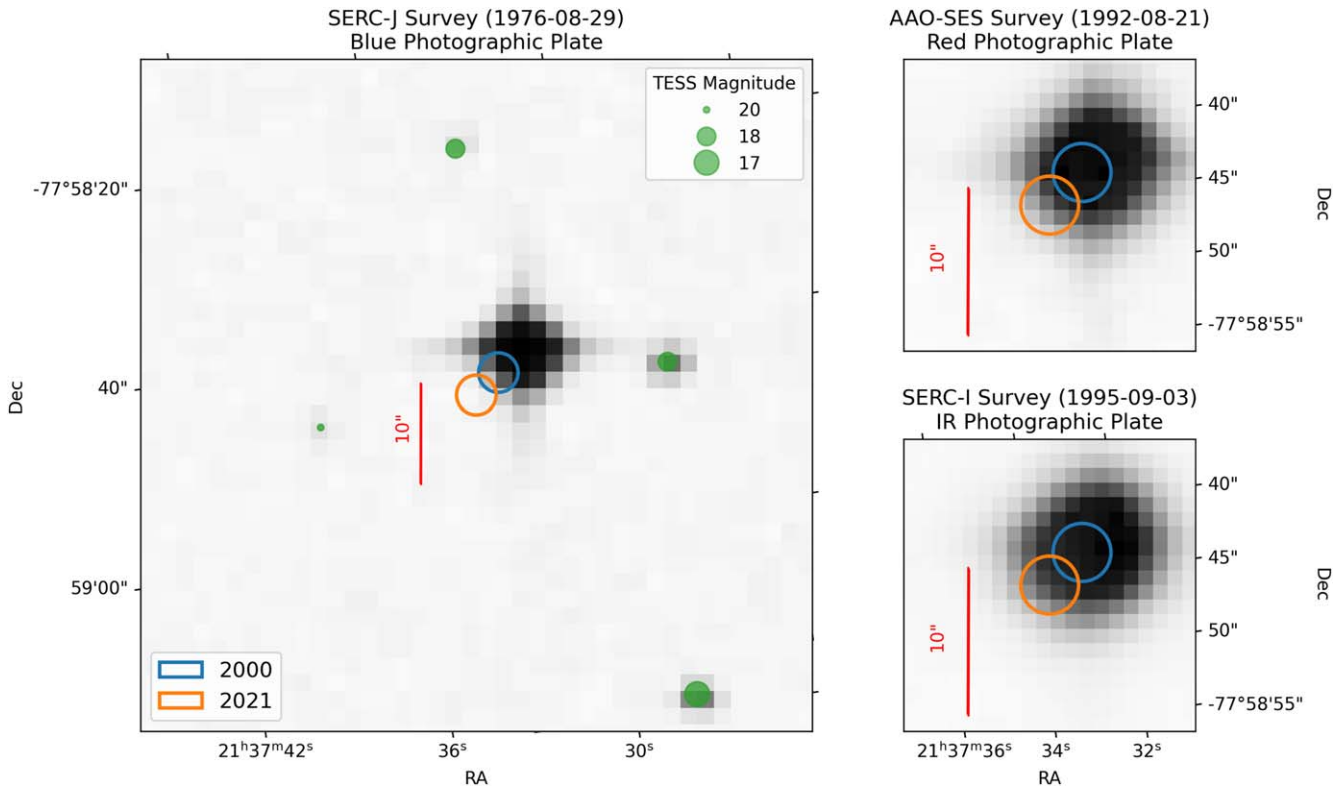


Figure 1. Images of the field surrounding TOI 4342 in 1976 (left), 1992 (top right), and 1995 (bottom right). In all images, the orange circle shows the 2021.0 location of TOI 4342 and the blue circle shows the location on J2000. Both circles have radii of $2''$. Nearby stars in the TIC are shown in green with marker size corresponding to brightness. In red is a $10''$ scale (\sim half a TESS pixel).

alerted as TOI 4342.01 and .02 on 2021 July 28 (Guerrero et al. 2021).

The FFIs meanwhile were reduced by QLP, but TOI 4342’s TESS band brightness is below the threshold to be released as a QLP TOI (10.5) (Guerrero et al. 2021). While developing the QLP improvements listed in Section 1, we conducted an independent search for multiplanet systems in QLP light curves and found two planet candidates in TOI 4342. For both sectors, our analysis started with raw QLP light curves, and uses calibrated FFIs from the MIT TESS image calibration software (TICA, Fausnaugh et al. 2020).²⁰ Figure 1 shows TOI 4342 and the surrounding field.

This multiplanet search consisted of iterative applications of the box least-squares algorithm (BLS, Kovacs et al. 2002) as implemented in VARTOOLS (Hartman & Bakos 2016), masking out transits for previously found signals when searching for new planets. We then also performed an additional step of light-curve detrending to remove short-timescale systematics. This was done by decorrelating spacecraft motion from the light curve using leading statistical moments (mean, standard deviation, skewness) of and covariances between the quaternion time series components Q1, Q2, and Q3 calculated within each exposure (Vanderburg et al. 2019). Together with basis splines to remove long-timescale trends (Vanderburg & Johnson 2014), we performed iterative fits to the light curve, removing 3σ outliers until the fit converged. The resulting combined trend was subtracted out to produce a final corrected QLP light curve.

With these adjustments, we found two signals. The first signal has a period of 5.538 days with S/N of 13.126 (5.14 per transit), and the second has a period of 10.688 days with S/N 11.506 (6.74 per transit). To highlight the impact of the First Extended Mission and QLP improvements, we specifically searched for planets in Sector 13 (Primary Mission) and Sector 27 (First Extended Mission) separately. Corrected for the number of transits seen in each sector, we saw average S/N per transit of 3.70 and 4.83 in Sector 13 for each signal respectively. In Sector 27, this improved to 5.52 and 5.99. We also compared the S/Ns with the original QLP detrending method (only correcting for long-timescale systematics) and found worse performance without the quaternion correction (S/Ns per transit of 5.07 and 5.32).

For the remainder of the system modeling in this work, we use the simple aperture photometry (SAP) light curve from the SPOC pipeline (Twicken et al. 2010; Morris et al. 2020) with the following preprocessing. First we removed contamination from nearby stars by scaling the light curves by the SPOC-provided CROWDSAP values. We also ignored data with nonzero SPOC quality flags. This included an anomalous event during Sector 13 (TJD 1665.2983 to 1665.3501) where the spacecraft fell out of fine pointing. The resulting light curve can be seen in Figure 2 with its Lomb–Scargle periodogram.

In the periodogram, we see a peak signifying stellar variability at a period of about 13 days. To remove this variability and other instrumental systematics, we conducted our own correction similar to our new QLP correction. First, we excluded data from QLP-predicted transit times, then we split the light curve into individual spacecraft orbits (with two orbits per sector) to be corrected separately. We again iteratively removed short-timescale systematics with quaternion time

²⁰ TICA FFIs are available as High Level Science Products at the Mikulski Archive for Space Telescopes (MAST): <https://archive.stsci.edu/hlsp/tica>.

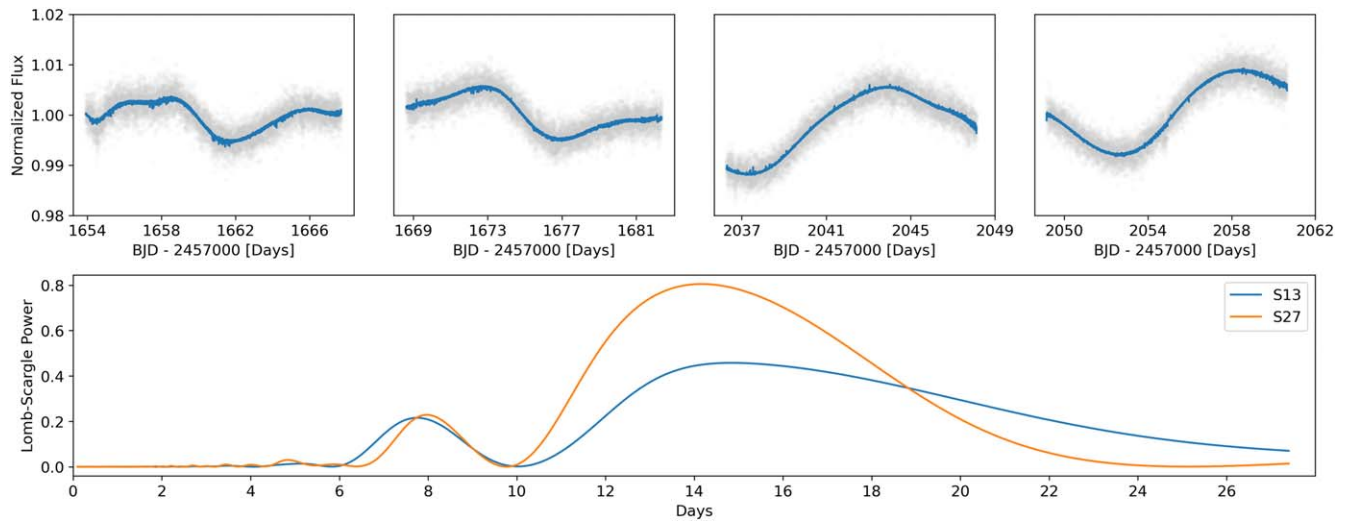


Figure 2. Top: SPOC SAP light curve with our correction trend (described in Section 2.1) in blue. This trend, formed from quaternion data and basis splines to remove systematics and long-timescale variability, is divided out of the raw light curve to create our final flattened light curve. Bottom: Lomb–Scargle periodograms of the SAP SPOC light curve for each sector of observation. We see peaks around 14 days marking stellar variability, but we cannot pin down a specific period due to the large gap between observations.

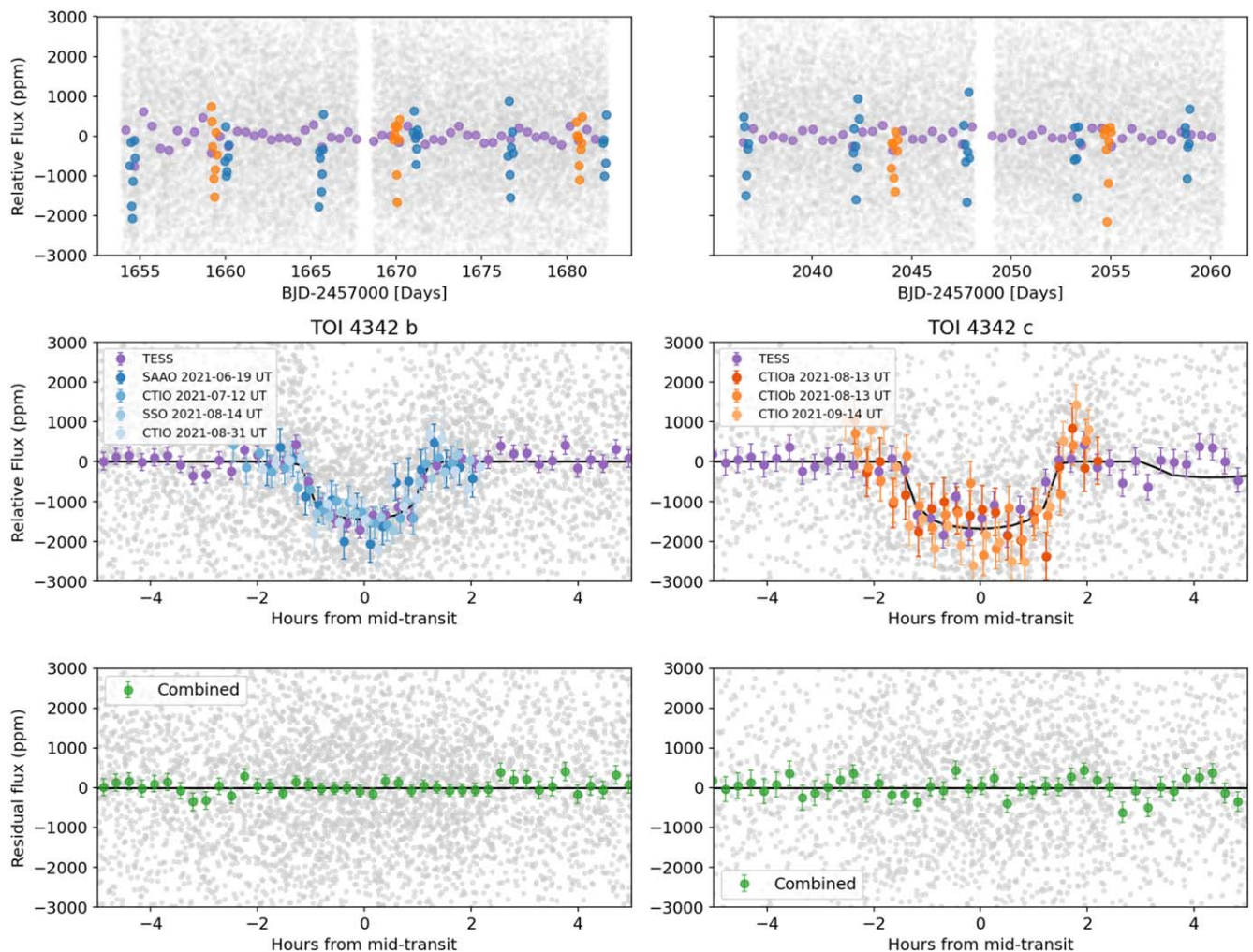


Figure 3. Top: detrended TESS light curve in gray, binned values in purple, with transits highlighted for each TOI 4342 b (blue) and TOI 4342 c (orange). Middle: TESS and LCOGT light curves folded on the best-fit period and epoch found in Section 3.2.1. Different background-subtracted observations are shown in different colors for each transit with the best-fit model in black. Bottom: residual flux between the fully combined light curve and the model.

Table 1
SG1 Follow-Up Observations

Target	Instrument	Date (UT)	Filter	Aperture	Observing Notes
TOI 4342 c	LCO-CTIO 1.0 m	2021-9-14	<i>i'</i>	5''1	
TOI 4342 b	LCO-CTIO 1.0 m	2021-8-31	<i>i'</i>	6''2	
TOI 4342 b	LCO-SSO 1.0 m	2021-8-14	<i>i'</i>	5''1	
TOI 4342 c	LCO-CTIO 1.0 m a	2021-8-13	<i>i'</i>	5''9	Simultaneous observation ^a
TOI 4342 c	LCO-CTIO 1.0 m b	2021-8-13	<i>i'</i>	5''9	Simultaneous observation ^a
TOI 4342 b	LCO-CTIO 1.0 m	2021-7-12	<i>i'</i>	6''2	
TOI 4342 c	LCO-SAAO 1.0 m	2021-7-11	<i>i'</i>	7''0	Noisy, cut short by weather
TOI 4342 b	LCO-SAAO 1.0 m	2021-6-19	<i>i'</i>	8''6	
TOI 4342 c	LCO-CTIO 1.0 m	2021-5-30	<i>i'</i>	7''8	Partial, cut short by weather

Note.

^a Transit observed simultaneously by two distinct telescopes at CTIO.

series statistics and long-timescale systematics with basis spline fits. This final fit was then divided out to produce our corrected light curve. Figure 3 shows the detrended 2 minutes cadence light curve with transits highlighted.

2.2. Ground-based Photometry

We obtained seeing-limited ground-based follow-up observations from the TESS Follow-up Observing Program Subgroup 1 (TFOP SG1; Collins 2019). The ground-based observations have much higher spatial resolution than TESS and can help confirm the source location of a TESS transit signal and can provide additional transit observations to refine ephemerides for predicting future transits. We used the TESS Transit Finder, which is a customized version of the Tapir software package (Jensen 2013), to schedule our transit observations.

Between 2021 May 30 and 2021 September 14 UT, four transits of TOI 4342 b and five transits of TOI 4342 c were observed in the Sloan *i'* band using the Las Cumbres Observatory Global Telescope (LCOGT; Brown et al. 2013) 1.0 m network. The observations were taken at the Siding Spring Observatory (SSO), South Africa Astronomical Observatory (SAAO), and Cerro Tololo Inter-American Observatory (CTIO) nodes of the LCOGT network and are summarized in Table 1. We use seven of the nine transits because two were cut short for bad weather conditions. The 1 m telescopes are equipped with 4096×4096 SINISTRO cameras having an image scale of $0''.389$ per pixel, resulting in a $26' \times 26'$ field of view. The images were calibrated by the standard LCOGT BANZAI pipeline (McCully et al. 2018). Differential photometric data were extracted with AstroImageJ (Collins et al. 2017) using circular photometric apertures with radii $6''.0$. Thus, the TOI 4342 aperture excludes flux from the nearest known Gaia DR3 and TIC v8 star (TIC 2025922721) $16''$ east of TOI 4342. As shown in Section 3.2, the transit signals are detected on-target relative to known Gaia DR3 stars. We also checked the light curves of Gaia DR3 sources within $2'.5$ of TOI 4342 and found no evidence of nearby eclipsing binary systems that could be causing the TESS detection. All SG1 data can be found online at ExoFOP (2019).

2.3. Reconnaissance Spectroscopy

We obtained nine spectra of TOI 4342 over two seasons in slicer mode with the fiber-fed high-resolution echelle spectrograph CHIRON (Tokovinin et al. 2013). CHIRON is mounted on the 1.5 m SMARTS telescope, located at the

Table 2
Radial Velocities of TOI 4342

BJD	RV (km s^{-1})	σ_{RV} (km s^{-1})	Instrument
2,459,359.91837	-5.726	0.013	CHIRON
2,459,360.85475	-5.760	0.018	CHIRON
2,459,379.77461	-5.795	0.020	CHIRON
2,459,384.82649	-5.770	0.011	CHIRON
2,459,409.75314	-5.788	0.012	CHIRON
2,459,700.86421	-5.734	0.018	CHIRON
2,459,725.87319	-5.747	0.016	CHIRON
2,459,740.83584	-5.737	0.016	CHIRON
2,459,742.79459	-5.761	0.012	CHIRON

CTIO, Chile, and has a spectral resolving power of 80,000. The spectra were taken using 1 hr long exposures and were extracted by the standard CHIRON pipeline (Paredes et al. 2021).

We derived the radial velocities (RVs) using a cross-correlation against a median-combined template spectrum. The template spectrum is composed of a median combination of all CHIRON spectra, each shifted to rest after an approximate velocity measurement via a cross-correlation against a synthetic template. The measured velocity of each spectrum is that of the mean velocity from each spectral order, weighted by the heights of their cross-correlation functions. The velocity uncertainties were estimated from the scatter of the per-order velocities. We find a mean internal uncertainty of $\sim 15 \text{ m s}^{-1}$, with an rms of $\sim 22 \text{ m s}^{-1}$ between the nine measurements. The full data set can be found in Table 2.

2.4. High-resolution Speckle Imaging

“Third-light” flux contamination from a close stellar companion can lead to an underestimated planetary radius if not accounted for in the transit model (Ciardi et al. 2015) and even cause nondetections of small planets residing within the same exoplanetary system (Lester et al. 2021). The discovery of close, bound companion stars, which exist in nearly one-half of FGK-type stars (Matson et al. 2018) and in fewer M-class stars, provides crucial information toward our understanding of exoplanetary formation, dynamics, and evolution (Howell et al. 2021). Thus, to search for close-in bound companions unresolved by TESS, Gaia, or ground-based seeing-limited follow-up observations, we obtained high-resolution speckle imaging observations of TOI 4342.

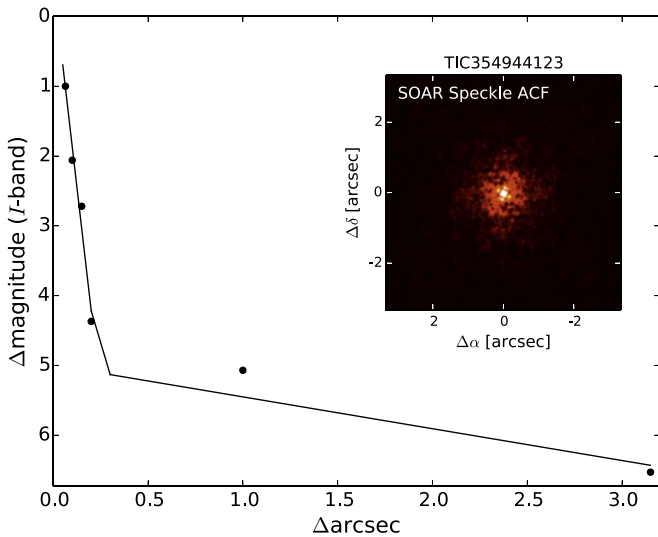


Figure 4. SOAR speckle autocorrelation function (inset plot) and its 5σ detection sensitivity curve (main plot) in the Cousins I band.

TOI 4342 was observed at the 4.1 m Southern Astrophysical Research (SOAR) telescope (Tokovinin 2018) on 2021 October 1 UT, in Cousins I band, a similar visible bandpass to TESS. This observation was sensitive to a 5 mag fainter star at an angular distance of $1''$ from the target. More details of the observations within this survey are available in Ziegler et al. (2020). The 5σ detection sensitivity and speckle autocorrelation functions from the observations are shown in Figure 4. No nearby stars were detected within $3''$ of TOI 4342 in the SOAR observations.

TOI 4342 was also observed on 2021 July 23 UT using the Zorro speckle instrument on the Gemini South 8 m telescope²¹ (Scott et al. 2021). Zorro provides simultaneous speckle imaging in two bands (562 nm and 832 nm) with output data products including a reconstructed image with robust contrast limits on companion detections (e.g., Howell et al. 2016). During this observing run, the blue channel was inoperable, thus only 832 nm observations were obtained. Thirteen sets of 1000×0.06 s exposures were collected and subjected to Fourier analysis in the standard reduction pipeline (see Howell et al. 2011). Figure 5 shows our final contrast curve and the 832 nm reconstructed speckle image. We find that TOI 4342 is a single star with no companion brighter than 5–6 mag below that of the target star from very close in ($0''.1$) out to $1''.2$. At the distance of TOI 4342 (61.54 pc) these angular distances correspond to spatial distances of 6.2–74 au.

3. Analysis

3.1. Stellar Parameters

We re-derive stellar parameters according to the following empirical relations. First we take the observed K_s magnitude from the Two Micron All Sky Survey (2MASS) and the parallax from the Gaia Data Release 3 (DR3, Gaia Collaboration et al. 2022) to find the absolute K_s magnitude of TOI 4342. Then, using the relation from Benedict et al. (2016), we get a stellar mass of $0.6296 \pm 0.0086 M_\odot$. With this mass, we use the mass–radius relation from Boyajian et al. (2012) to find a stellar radius of $0.599 \pm 0.013 R_\odot$. We check this with the

absolute K_s magnitude–radius relation from Mann et al. (2015), where we find a consistent value of $0.598 \pm 0.018 R_\odot$. From Mann et al. (2015), we also calculate a bolometric luminosity of $0.0746 \pm 0.0053 L_\odot$ via the observed V and J magnitudes and the resulting bolometric correction. Using the Stefan–Boltzmann law, we find an effective temperature of 3901 ± 69 K, giving TOI 4342 a spectral type around M0V. These values are consistent with the stellar parameters listed in TIC 8.2 of $0.587 \pm 0.020 M_\odot$, $0.598 \pm 0.018 R_\odot$, $0.073 \pm 0.016 L_\odot$, and 3880 ± 160 K, which were derived using the older Gaia DR2.

3.2. Light-curve Modeling

3.2.1. Best-fit Model

We simultaneously fit the detrended TESS light curve and all seven of the nine SG1 light curves unaffected by weather (see Table 1) using *exoplanet* (Foreman-Mackey et al. 2021).

For TESS light curves, we approximate the per-point measured uncertainty as 1.4826 times the median absolute deviation of the flux within each TESS orbit. For each SG1 light curve, we use the reported flux uncertainties, and on top of that we fit for a jitter term (added in quadrature) to capture additional errors in the observation’s error budget. We also simultaneously fit a second-order polynomial to the SG1 light curves to account for nightly trends. To model the stellar limb darkening we use quadratic limb-darkening models with uninformative priors following Kipping (2013a) for each observation band.

For both orbits, we assume an eccentricity of 0.²² Periods and epochs for each planet were given uniform priors centered on the values found via BLS search to $\pm 10\%$ of the period. The ratios of planet to stellar radii had uniform priors from 0 to 1, and impact parameters had uniform priors from $-(1 + R_p/R_*)$ to $+(1 + R_p/R_*)$ (though when reported, we take the absolute value). Finally, the stellar mass and radius were given normal priors using the parameters derived in Section 3.1.

exoplanet uses PyMC3 (Salvatier et al. 2016) to perform No U-turn Sampling (Hoffman & Gelman 2011) from the posterior distribution. We sampled five independent chains with 5000 tuning steps and 5000 draws. All parameters converged with Gelman–Rubin statistic ≤ 1.01 (Gelman & Rubin 1992). Table 3 shows the median sampled and derived values with 1σ confidence intervals, and Figure 3 shows the median posterior model with residuals.

3.2.2. Transit Shape Model

Separately, using *exoplanet*’s SimpleTransitOrbit we also performed a TESS-only fit to best constrain each candidate’s transit shape—the ratio between the duration of the flat part of the transit (t_F) and the total transit duration (t_T).

Again, we assume a Gaussian noise model on top of a constant baseline. Priors on period and epoch were set to uniform distributions centered around the BLS periods and epochs with bounds of $\pm 10\%$ of the period. Durations were given uniform priors from 0 to 2 times the BLS durations, R_p/R_* was given uniform priors from 0 to 1, and impact parameters were given uniform priors from $-(1 + R_p/R_*)$ to $+(1 + R_p/R_*)$. Since we want to find the best characterization

²¹ <https://www.gemini.edu/sciops/instruments/alopeke-zorro/>

²² Based on priors from Kipping (2013b) and Eyles et al. (2019), we expect the eccentricities to be low. We also performed a separate fit with an uninformed prior on the eccentricity and argument of periaapsis, and did not see significant changes in the results.

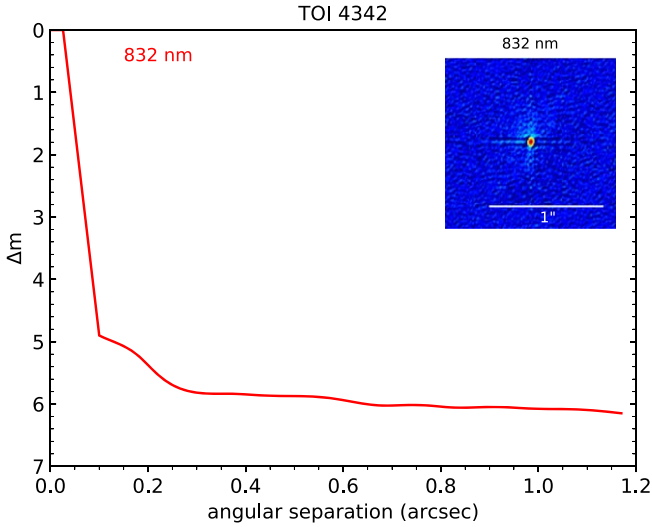


Figure 5. Gemini South Zorro speckle imaging 5σ contrast curve (full plot) and reconstructed images (inset plot) in the 832 nm band. The diffraction limit of the instrument is 20 mas.

of the transit shape for each planet independently from the host star, we use two independent star models with loose stellar radius priors from 0 to $2 R_{\odot}$ and quadratic limb darkening with Kipping (2013a)’s priors.

Following the same fitting configuration as Section 3.2.1, we can calculate the transit shape following Equation (15) from (Seager & Mallen-Ornelas 2003):

$$\left(\frac{t_F}{t_T}\right)^2 = \frac{(1 - R_p/R_*)^2 - b^2}{(1 + R_p/R_*)^2 - b^2}, \quad (1)$$

where R_p is planet radius, R_* is stellar radius, and b is impact parameter. For TOI 4342 b and TOI 4342 c respectively, we find median and 1σ confidence intervals of $0.912^{+0.013}_{-0.026}$ and $0.907^{+0.016}_{-0.039}$.

3.3. Radial Velocity Modeling

Using the CHIRON data (Table 2), we can place upper limits on the mass of both planets by fitting for the amplitudes of simple sinusoids assuming circular orbits. This puts an upper bound on the variations in radial velocity, meaning we can constrain the mass of any transiting companion to be planetary rather than stellar.

We define our model with three unknowns: the baseline radial velocity, K_b , and K_c , where the K ’s are semiamplitudes of sinusoids set to the median periods and epochs from Section 3. After fitting, we find semiamplitudes of $19.4^{+5.1}_{-5.0}$ m s^{-1} and $14.4^{+3.6}_{-3.6}$ m s^{-1} for each signal respectively. These posteriors give us 3σ mass upper limits of $0.321 M_{\text{Jup}}$ and $0.289 M_{\text{Jup}}$, both much smaller than stellar masses.

3.4. Photocenter Motion

Photocenter motion analysis can help determine whether the location of a transit signal matches the location of the target star on the sky.

An effective method of determining both of these locations is with the difference imaging technique (Bryson et al. 2013), designed initially for the Kepler mission and inherited by the SPOC pipeline, whereby the difference of averaged in- and out-

Table 3
Stellar and Planet Parameters for TOI 4342

Parameter	Value	Source
Catalog information		
R.A. (h:m:s)	21:37:33.48	Gaia DR3
decl. (d:m:s)	-77:58:44.9743	Gaia DR3
Epoch	2016.0	Gaia DR3
Parallax (mas)	16.249 ± 0.018	Gaia DR3
$\mu_{\text{R.A.}}$ (mas yr $^{-1}$)	120.333 ± 0.019	Gaia DR3
$\mu_{\text{decl.}}$ (mas yr $^{-1}$)	-91.503 ± 0.018	Gaia DR3
Gaia DR3 ID	6355915466181029376	
TIC ID	354944123	
TOI ID	4342	
Photometric properties		
TESS (mag)	11.0318 ± 0.0074	TIC v8.2
Gaia (mag)	11.97403 ± 0.00032	Gaia DR3
Gaia RP (mag)	11.02247 ± 0.00081	Gaia DR3
Gaia BP (mag)	12.8963 ± 0.0014	Gaia DR3
V_J (mag)	12.669 ± 0.057	UCAC4 ^a
B_J (mag)	14.055 ± 0.011	APASS DR9 ^b
J (mag)	9.832 ± 0.024	2MASS
H (mag)	9.179 ± 0.024	2MASS
K_s (mag)	9.018 ± 0.021	2MASS
Derived properties		
M_* (M_{\odot})	0.6296 ± 0.0086	Parallax + Benedict et al. (2016) ^c
R_* (R_{\odot})	0.599 ± 0.013	Parallax + Mann et al. (2015) ^d
$\log g_*$ (cgs)	$4.6878^{+0.0086}_{-0.0096}$	empirical relation + LC ^e
L_* (L_{\odot})	0.0746 ± 0.0053	Mann et al. (2015)
$T_{\text{eff},*}$ (K)	3901 ± 69	f
M_V (mag)	14.39 ± 0.02	Parallax
M_K (mag)	8.272 ± 0.015	Parallax
Distance (pc)	61.543 ± 0.070	Parallax
ρ_* (g cm^{-3})	$2.985^{+0.089}_{-0.097}$	empirical relation + LC ^e
Limb-darkening coefficients		
u_1 , TESS	$0.27^{+0.13}_{-0.11}$	
u_2 , TESS	$0.37^{+0.17}_{-0.18}$	
u_1 , i'	$0.44^{+0.13}_{-0.14}$	
u_2 , i'	$0.08^{+0.18}_{-0.17}$	
Light-curve parameters		
P (days)	TOI 4342 b $5.5382498^{+0.0000057}_{-0.0000058}$	TOI 4342 c $10.688716^{+0.000015}_{-0.000015}$
T_c (BJD - 2,457,000)	$1654.53559^{+0.00059}_{-0.00061}$	$1659.34623^{+0.00096}_{-0.00094}$
T_{14} (hr)	$2.215^{+0.020}_{-0.018}$	$2.820^{+0.024}_{-0.025}$
$T_{12} = T_{34}$ (min)	$4.88^{+0.15}_{-0.13}$	$6.31^{+0.16}_{-0.14}$
a/R_*	$18.97^{+0.19}_{-0.21}$	$29.40^{+0.29}_{-0.32}$
R_p/R_*	$0.03491^{+0.00047}_{-0.00049}$	$0.03719^{+0.00054}_{-0.00057}$
$b \equiv a \cos i/R_*$	$0.290^{+0.042}_{-0.050}$	$0.187^{+0.060}_{-0.061}$
i (deg)	$89.13^{+0.15}_{-0.13}$	$89.63^{+0.12}_{-0.12}$
Planetary parameters		
R_p (R_{\oplus})	$2.266^{+0.038}_{-0.038}$	$2.415^{+0.043}_{-0.040}$
a (au)	$0.05251^{+0.00011}_{-0.00011}$	$0.08140^{+0.00017}_{-0.00017}$
T_{eq} (K)	$633.6^{+6.2}_{-6.3}$	$508.9^{+5.0}_{-5.0}$
$\langle F \rangle$ (S_{\oplus})	$26.9^{+1.1}_{-1.0}$	$11.18^{+0.45}_{-0.44}$

Notes.

^a Zacharias et al. (2013).

^b Henden et al. (2016).

^c We adopt error based on the scatter in the empirical relations from Benedict et al. (2016).

^d We adopt error based on the scatter in the empirical relations from Mann et al. (2015).

^e We fitted the transit light curves with a prior constraint on the stellar density.

^f T_{eff} was determined from the bolometric luminosity and the stellar radius.

of-transit pixel images is found. Assuming stellar variability and/or instrumental systematics are negligible on transit timescales, the difference image should appear starlike at the location of the transit signal source. Meanwhile, the out-of-transit image should represent a direct image of the field

surrounding the target star. If the field is relatively uncrowded and the target star is indeed the source of the transit signal, the difference and direct images should appear similar.

To produce difference and direct images, we used `TESS-plots`,²³ a publicly available Python package for robust pixel-level analysis of TESS FFIs. For planets in multiplanet systems such as TOI 4342, `TESS-plots` masks out all cadences corresponding to other planet transits. This ensures that the primary source of variability in the difference image is due to the planet of interest. `TESS-plots` also puts more care in choosing which in- and out-of-transit frames are used than the original difference images in QLP. It ignores the first and last 5% of the transit duration to better avoid ingress/egress. It also places a buffer between in- and out-of-transit frames to handle underestimated transit durations. Finally, “bad” transits (transits with lots of missing or poor-quality data points) are discarded to prevent contamination of the overall difference image. Altogether, with these improvements, `TESS-plots` marks an important update over the Primary Mission QLP difference images.

Figure 6 shows difference images for TOI 4342 b and TOI 4342 c next to the direct image for TOI 4342, using Sector 27 FFIs. The difference images confidently rule out the transit signals as coming from other nearby sources listed in the TIC, consistent with the centroid analysis derived by the SPOC pipeline. For TOI 4342 b, the SPOC-derived photocenter is only 2.5σ away from the location of TIC 2025922721 ($T = 19.805$ mag). However, this star is too faint to produce the transit depths observed on TOI 4342.

3.5. Possible False Positive Scenarios

In this section we rule out possible false positive scenarios where the signals are not coming from a multiplanet system.

3.5.1. TOI 4342 is an Eclipsing Star System

One possible source of false positives could be signals from eclipsing stellar companions rather than planetary companions. We can rule out this scenario by considering our radial velocity model in Section 3.3. We found 3σ upper limits on semiamplitude magnitudes of 50 m s^{-1} and 36 m s^{-1} , which translate to mass limits of $0.321 M_{\text{Jup}}$ and $0.289 M_{\text{Jup}}$ for TOI 4342 b and TOI 4342 c respectively. In other words, if our transit signals are caused by gravitationally bound companions that block out light from TOI 4342, those companions must have sub-Jupiter masses and cannot be stars.

3.5.2. Contamination from a Nearby Eclipsing Binary

Another major source of false positives is the signal of an eclipsing binary (EB) in the field near our target of interest. Because photometers measure all light within a specific aperture, eclipses from a nearby EB (NEB) can contaminate the target aperture and cause transit-like events in the light curve. These false positives account for as much as 40% of transit-like signals at the lowest Galactic latitudes in the Kepler field (Morton & Johnson 2011; Bryson et al. 2013).

We can start ruling out NEBs by restricting the signal source to be near TOI 4342. Our photocenter motion analysis in Section 3.4 rules out signals from known TIC v8 stars, constraining the signal to be within $\sim 21''$ (one TESS pixel) of

TOI 4342. In Section 2.2, SG1 observations rule out signals from the nearest Gaia DR3 stars. In DR3 (Fabricius et al. 2021; Gaia Collaboration et al. 2022), Gaia has a resolution down to $\sim 0''.7$, so the signal must be on-target or from an NEB within an arcsecond of TOI 4342.

Next, we can rule out potential NEBs by showing they must be brighter than certain magnitudes to cause either transit signal. First, we note the observed transit depth δ_{obs} is

$$\delta_{\text{obs}} = \delta_{\text{EB}} \cdot \frac{f}{1+f}, \quad (2)$$

where δ_{EB} is the “true” depth (the NEB’s primary eclipse depth if TOI 4342 were not present), and f is the flux ratio between the NEB and TOI 4342.

Then, we can place an upper bound on δ_{EB} by assuming $b=0$ as in Equation (21) from Seager & Mallen-Ornelas (2003):

$$\delta_{\text{EB}} \leq \frac{(1 - t_F/t_T)^2}{(1 + t_F/t_T)^2}. \quad (3)$$

Together with Equation (2), this places a lower bound on f purely as a function of δ_{obs} and transit shape (t_F/t_T):

$$\frac{\delta_{\text{obs}}/\delta_{\text{EB}}}{1 - \delta_{\text{obs}}/\delta_{\text{EB}}} \leq f, \quad (4)$$

which we can rearrange to an upper bound on NEB magnitude ($m_{\text{EB}} - m_* = -2.5 \log_{10} f$ where m_* is 11.032, the T_{mag} of TOI 4342).

Using the result of the transit shape model in Section 3.2.2, we can derive 3σ lower bounds on transit shape for each signal. These correspond to upper bounds on NEB magnitude of 15.38 and 16.70 ($\Delta T = 4.35$ and 5.67 mag). In other words, for an NEB to cause the TOI 4342 b signal, it is likely within 4.35 mag of TOI 4342.

In Figure 4, we see no stars within 5–6 mag of TOI 4342 at separations of $1''$ – $3''$. This supports the ruling-out of Gaia sources down to around $1''$. In Figure 5, no neighbors within 5–6 mag of TOI 4342 were detected from $0''.1$ to $1''.2$. So, altogether we can rule out NEBs greater than $0''.1$ away from TOI 4342 as sources of the transit signals.

Lastly, taking advantage of the relatively high proper motion of TOI 4342, we can use archival images to rule out NEBs within $0''.1$ of TOI 4342’s current location. Figure 1 shows the field surrounding TOI 4342 in 1976 along with all known nearby TIC stars for magnitude reference. We see that in 1976, the 2021 location of TOI 4342 is clear of any stars with $T_{\text{mag}} \lesssim 17$ ($\Delta T \simeq 6$ mag). This rules out NEBs within $0''.1$ of TOI 4342.

Altogether, using our photocenter motion analysis, high-resolution speckle imaging, and archival field images, we are able to rule out contamination from an NEB as the source of either transit signal.

3.5.3. TOI 4342 is a Hierarchical Triple

The final scenario we consider is an EB gravitationally bound to TOI 4342 (i.e., a hierarchical triple system). This EB would cause the same aperture contamination described in Section 3.5.2 (with the same magnitude limits), but could have evaded detection in Figure 1 because it would stay close to TOI 4342.

²³ <https://github.com/mkunimoto/TESS-plots>

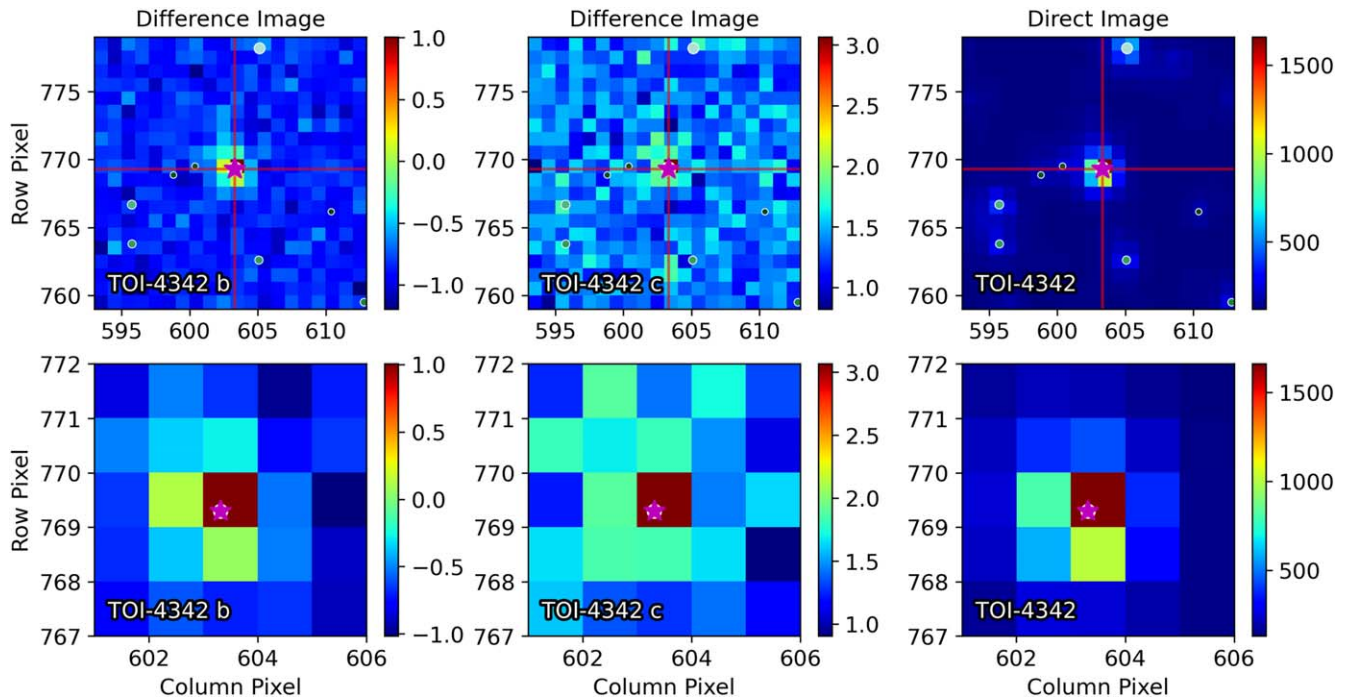


Figure 6. Difference images for TOI 4342 b and TOI 4342 c, made using 20×20 pixel cutouts of the Sector 27 TESS FFIs (top). A close-up of the central 5×5 pixels is also shown (bottom). The third column shows the average of out-of-transit images, which should represent a direct image of the field near the target star. The target TIC 354944123 is indicated with a pink star, while nearby stars down to $\Delta T = 4$ mag are plotted as white circles with sizes scaled by brightness. The difference images for both planet candidates indicate the transit sources are collocated with the target star. The color bars are all in units of electrons per second.

In this scenario, if we assume the EB’s orbit is within $0''.1$ of TOI 4342, its semimajor axis would be at most ~ 6.2 au (at a distance of 61.54 pc via Gaia DR3 parallax). With Kepler’s third law and the stellar mass from Section 3.1, this gives the NEB an orbital period of ~ 19.2 yr around TOI 4342.

From Section 3.5.2, we saw that NEBs should be brighter than $\Delta T \simeq 5$ mag to cause the transit signals. This translates to a minimum luminosity of $7.5 \times 10^{-4} L_{\odot}$ and, using $L \propto M^{3.5}$, a minimum mass of $0.13 M_{\odot}$.

For a gravitationally bound NEB with a mass of at least $0.13 M_{\odot}$, we would expect an edge-on radial velocity semi-amplitude of $\sim 1.8 \text{ km s}^{-1}$. Gaia DR3 observed TOI 4342 over a 34 month baseline. In this timeframe, if there were a $0.13 M_{\odot}$ companion at 6.2 au, we would expect an RV shift of $\sim 1 \text{ km s}^{-1}$. The reported mean RV error though is only $\sim 0.36 \text{ km s}^{-1}$. Similarly, from Section 3.3, our RV data span more than a year. Based on this observation timeline, we expect an RV scatter from a companion NEB at a distance of 6.2 au with $0.13 M_{\odot}$ would be larger than our observed 22 m s^{-1} at least 95% of the time.

Together, since the actual RV error is lower than expected from a companion EB for both our RV data and Gaia data, we conclude that these scenarios of EBs gravitationally bound to TOI 4342 are unlikely causes of the transit signals.

3.5.4. TRICERATOPS and Summary

Using two sectors of TESS data along with additional photometric and spectroscopic observations, we were able to rule out most astrophysical false positives as sources of our transit signals. We considered the possibilities that our signals are caused directly by an EB, by contamination from a background EB, and by certain configurations of a hierarchical companion EB. For each scenario, we showed that it is highly

unlikely for that scenario to cause our transits. In addition, we use *triceratops* (Giacalone & Dressing 2020) to independently check the false positive probabilities (FPPs) and nearby false positive probabilities (NFPPs) for each signal. After 20 runs for each signal, we calculate mean and standard deviation FPPs of 0.00211 ± 0.00018 and 0.00320 ± 0.00027 , and NFPPs of 0.0000138 ± 0.0000013 and 0.000387 ± 0.000026 . Finally, Lissauer et al. (2012) and Guerrero et al. (2021) found that multicandidate systems have *lower* false positive rates than single-candidate systems, so we receive a “multiplicity boost,” further decreasing the false positive probabilities and increasing the likelihood of having real planets. Altogether, we conclude that our signals are statistically valid exoplanet transits.

4. Results and Discussion

In this work, we statistically validated a pair of sub-Neptunes around M0V dwarf TOI 4342. In this section, we discuss this system in the context of other planetary systems.

4.1. Follow-up Characterization of Mass and Atmosphere

The best-fit parameters from Section 3.2.1 show the planets have radii of $2.266^{+0.038}_{-0.038}$ and $2.415^{+0.043}_{-0.040} R_{\oplus}$, and periods of 5.538 and 10.689 days. Given their radii, these planets are most likely sub-Neptunes with a significant fraction of H/He in their atmospheres (Rogers 2015). Using the sub-Neptune mass–radius relationship from Wolfgang et al. (2016), we expect the planets to have masses of $7.83^{+0.93}_{-0.88}$ and $8.53^{+0.90}_{-0.94} M_{\oplus}$.

This corresponds to expected radial velocity semi-amplitudes of 3.9 and 3.4 m s^{-1} , meaning it is feasible to measure the precise masses using a high-precision radial velocity instrument mounted on a large telescope for TOI 4342 ($V = 12.67$ mag). With these masses, we will be able to compare bulk densities of the planets. Given the similar radii (within 10% of each other),

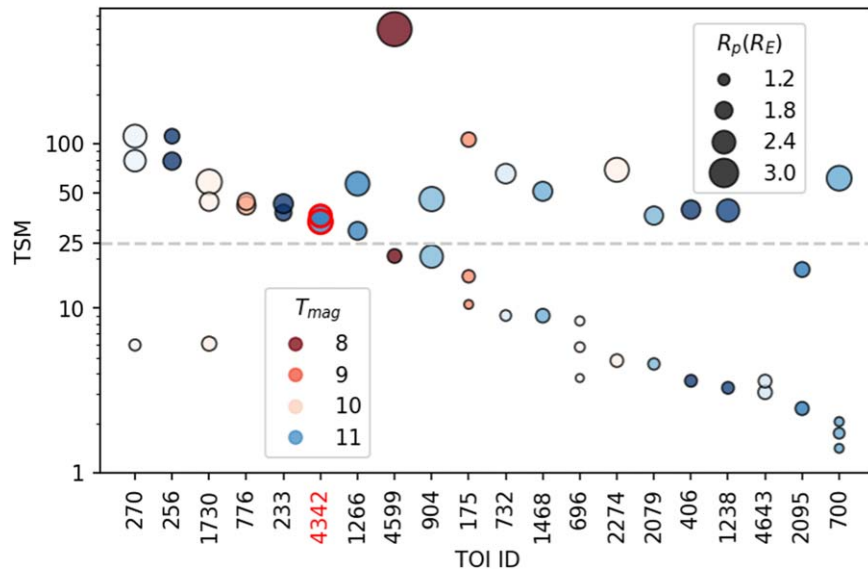


Figure 7. TSM, as defined in Kempton et al. (2018), for TOIs in multiplanet systems around bright M dwarfs ($T_{\text{eff}} < 4000$ K and $T_{\text{mag}} < 11.5$) with $R_p < 4 R_{\oplus}$ as of 2022 July 7. TIC stars are sorted in decreasing order of second largest TSM value in the system. Color corresponds to host T_{mag} and size corresponds to planet radius. The gray dashed line is the atmospheric follow-up threshold recommended by Guerrero et al. (2021) for sub-Neptunes. TOI 4342 is among the top 10 systems with multiple planets that are well suited for atmospheric characterization.

this will show the influence of different levels of irradiation (incident fluxes of ~ 27 and $\sim 11 S_{\oplus}$) on the planet atmospheres.

Using the expected masses, we can also calculate transmission spectroscopy metrics (TSMs, Kempton et al. 2018), measures of how promising planets are for atmospheric characterization studies. For these planets, we find values of 36 and 32, both of which are above the updated follow-up threshold of ~ 25 recommended by Guerrero et al. (2021) for the 100 best atmospherically characterizable sub-Neptunes (updated from Kempton et al. 2018).

More notably, TOI 4342 has *multiple* (more than one) high-TSM planets, making it one of the best M-dwarf systems for atmospheric comparison studies. Figure 7 shows the TSM values for multiplanet M-dwarf systems sorted by second highest TSM value of planets in each system. Characterizing and comparing the atmospheres of both planets will allow us to perform comparative exoplanetology, and TOI 4342 is one of the few systems where multiple planets have characterizable atmospheres. Additionally, given the two planets are near a mean-motion resonance (MMR) of 2:1, it is likely they migrated together to their current orbits and have similar primordial compositions. This would mean any differences detected in their atmospheric properties can probably be attributed to the differing levels of stellar irradiation between the planets. This will help us gain insights into the evolution of planetary atmospheres and responses to different intensities of stellar irradiation.

4.2. Radius Gap for Small Planets

Fulton et al. (2017) identified a radius gap for small planets roughly between 1.5 and $2.0 R_{\oplus}$, separating rocky super-Earths and gaseous sub-Neptunes for Sun-like stars. Cloutier & Menou (2020) showed this gap persisted around low-mass stars. One predominant cause of this gap may be photo-evaporation: the stripping away of a planet’s atmosphere as it undergoes heavy irradiation from its star (Owen & Wu 2013). Highly irradiated planets would be left as bare rocky cores,

while less irradiated planets would keep their atmospheres with larger mass and radii, leading to a bimodal radius distribution. With radii of 2.27 and $2.41 R_{\oplus}$, both TOI 4342 b and TOI 4342 c appear to fall on the upper side of the valley. Figure 8 shows TOI 4342 b and TOI 4342 c in cyan as a function of irradiation level and planetary radius over relative occurrence contours from Fulton & Petigura (2018). We see both planets have relatively low irradiation levels of ~ 27 and $\sim 11 S_{\oplus}$ respectively, meaning they are likely good fits for their description as low-mass atmosphere-retaining sub-Neptune planets on the upper side of the gap.

4.3. Transit Timing Variation (TTV)

With periods of 5.538 days and 10.689 days, TOI 4342 b and TOI 4342 c also fall within 5% of the first-order MMR of 2:1. Given the proximity to the 2:1 resonance, we expect the system would show transit timing variation (TTV) signals. Based on formulae in Lithwick et al. (2012), the super period of the TTV is about 157 days; the amplitude of the TTV signal is expected to be of the order of a few minutes using the estimated mass from empirical relations. Calculations using TTVFast (Deck et al. 2014) assuming the expected planet masses and eccentricities smaller than 0.1 for both planets show similar results to Lithwick et al. (2012). For TOI 4342, the photometric observations from ground-based 1 m telescopes were able to achieve transit time measurements at a similar or slightly better precision than TESS. With these observations, we can search for evidence of TTVs over a baseline of >800 days via exoplanet’s TTVOrbit. First, we subtract the best-fit background trends found in Section 3.2.1 from each light curve. We use the global best-fit ephemerides to set normal priors on transit times with standard deviations of 7 minutes. The rest of the parameters (limb darkening, stellar properties, radii ratios, impact parameter) are initialized following the best-fit model. Sampling parameters similarly followed the best global fit model. Based on the TTV fit, we do not observe significant deviation from linear ephemerides by more than 5 minutes for a majority of the observations (Figure 9), indicating

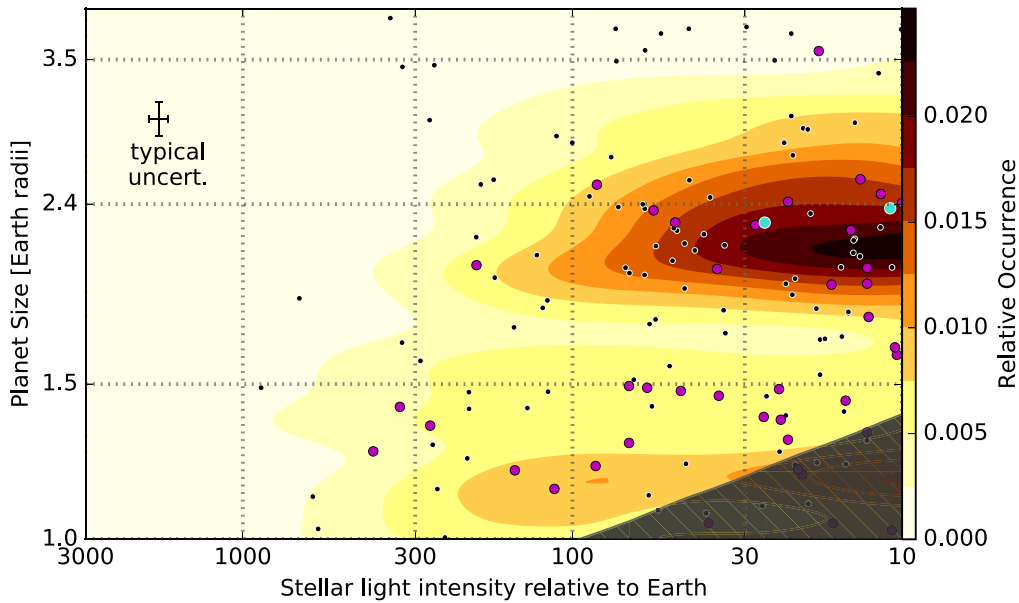


Figure 8. Insolation and orbital period vs. planet size. TOI 4342 b and TOI 4342 c are shown in cyan over occurrence contours for host stars with $M_* < 0.97 M_\odot$ from Fulton & Petigura (2018). M-dwarf TOIs as of 2022 July 7 are plotted as well, with multiplanet system planets highlighted in magenta. TOI 4342 b and TOI 4342 c both lie in the upper end of the radius valley.

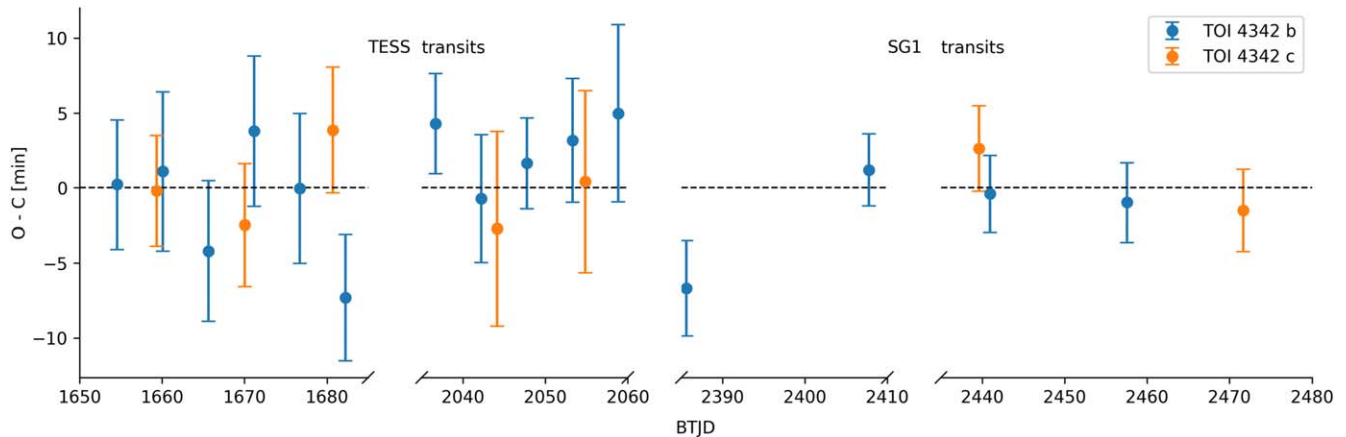


Figure 9. Observed minus calculated transit times for all observed transits across TESS and SG1 data. Observed transit times were modeled with `exoplanet's` `TTVOrbit` (Section 4.3) and the expected transit times were linearly propagated from the best-fit ephemerides (Section 3.2.1). Based on the current data, we see no evidence for significant deviations from expected transit times. With expected TTV amplitudes of only ~ 5 minutes, future observations could help pinpoint TTV amplitudes.

that the eccentricities of both planets are likely to be close to zero. TESS will reobserve TOI 4342 in Sectors 66 and 67 (2023 June–July), adding new transits that will help further constrain the TTV amplitudes. Additional photometric observations that can achieve transit center timing with precision better than 1 minute can also provide stronger constraints on the TTV amplitudes. If measured, these amplitudes could help constrain planet masses.

4.4. QLP and Extended Mission FFIs

This discovery showcases our recent improvements to QLP on Extended Mission FFIs. By adding a multiplanet search, short-timescale systematic correction, and improved difference images to QLP, we were able to detect this new M-dwarf system using the First Extended Mission FFIs. We saw improvements in signal-to-noise ratio when comparing transit searches between the original detrending method and the improved method. We also saw improvements when

comparing searches between the Primary Mission and Extended Mission FFIs. On top of this, the multiplanet search, together with the longer light-curve baseline, let us discover *both* planets in the system, where the original QLP would only have found one. Finally, we were able to use the improved difference images in localizing the source of the transit events to our particular target.

TOI 4342 is just one example of systems we will be able to find with all these improvements. In the future, we expect these upgrades to yield even more multiplanet M-dwarf systems as they continue to be used with every new sector of the standard QLP planet detection procedures at MIT. This will help build up our populations of small planets that are suitable for follow-up.

This paper includes data collected by the TESS mission, which are publicly available from the Mikulski Archive for Space Telescopes (MAST; Huang 2020; Fausnaugh 2021;

Team 2021). Funding for the TESS mission is provided by NASA's Science Mission directorate. We acknowledge the use of public TESS data from pipelines at the TESS Science Office and at the TESS Science Processing Operations Center. Resources supporting this work were provided by the NASA High-End Computing (HEC) Program through the NASA Advanced Supercomputing (NAS) Division at Ames Research Center for the production of the SPOC data products. This research has made use of the Exoplanet Follow-up Observation Program website (ExoFOP 2019), which is operated by the California Institute of Technology, under contract with the National Aeronautics and Space Administration under the Exoplanet Exploration Program. This research has made use of the NASA Exoplanet Archive, which is operated by the California Institute of Technology, under contract with the National Aeronautics and Space Administration under the Exoplanet Exploration Program.




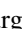

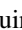


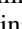
Some of the observations in the paper made use of the High-Resolution Imaging instrument Zorro obtained under Gemini LLP Proposal Number: GN/S-2021A-LP-105. Zorro was funded by the NASA Exoplanet Exploration Program and built at the NASA Ames Research Center by Steve B. Howell, Nic Scott, Elliott P. Horch, and Emmett Quigley. Zorro was mounted on the Gemini South telescope of the international Gemini Observatory, a program of NSF's OIR Lab, which is managed by the Association of Universities for Research in Astronomy (AURA) under a cooperative agreement with the National Science Foundation. on behalf of the Gemini partnership: the National Science Foundation (United States), National Research Council (Canada), Agencia Nacional de Investigación y Desarrollo (Chile), Ministerio de Ciencia, Tecnología e Innovación (Argentina), Ministério da Ciência, Tecnologia, Inovações e Comunicações (Brazil), and Korea Astronomy and Space Science Institute (Republic of Korea).













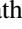





This work makes use of observations from the LCOGT network. Part of the LCOGT telescope time was granted by NOIRLab through the Mid-Scale Innovations Program (MSIP). MSIP is funded by NSF.

Facilities: TESS, Gaia, CTIO:1.5m (CHIRON), LCO:1.0m (Sinistro), SOAR:4.1m (HRCam), Gemini South:8m (Zorro).

Software: AstroImageJ (Collins et al. 2017), Astropy (Collaboration et al. 2013; Astropy Collaboration et al. 2018), exoplanet (Kipping 2013a; Salvatier et al. 2016; Theano Development Team et al. 2016; Kumar et al. 2019; Luger et al. 2019; Agol et al. 2020; Foreman-Mackey et al. 2021), H5py, Matplotlib (Hunter 2007), MIT Quick Look Pipeline (Huang et al. 2020a), Numpy (Harris et al. 2020), TESS SPOC Pipeline (Jenkins et al. 2016; Li et al. 2018; Twicken et al. 2018), Pandas (Reback et al. 2020), Scipy (Virtanen et al. 2020), Vartools (Hartman & Bakos 2016).

ORCID iDs

Evan Tey  <https://orcid.org/0000-0002-5308-8603>
 Chelsea X. Huang  <https://orcid.org/0000-0003-0918-7484>
 Michelle Kunitomo  <https://orcid.org/0000-0001-9269-8060>
 Andrew Vanderburg  <https://orcid.org/0000-0001-7246-5438>
 Avi Shporer  <https://orcid.org/0000-0002-1836-3120>
 Samuel N. Quinn  <https://orcid.org/0000-0002-8964-8377>
 George Zhou  <https://orcid.org/0000-0002-4891-3517>
 Karen A. Collins  <https://orcid.org/0000-0001-6588-9574>
 Kevin I. Collins  <https://orcid.org/0000-0003-2781-3207>

Eric L. N. Jensen  <https://orcid.org/0000-0002-4625-7333>
 Richard P. Schwarz  <https://orcid.org/0000-0001-8227-1020>
 Tianjun Gan  <https://orcid.org/0000-0002-4503-9705>
 Elise Furlan  <https://orcid.org/0000-0001-9800-6248>
 Crystal L. Gnilka  <https://orcid.org/0000-0003-2519-6161>
 Steve B. Howell  <https://orcid.org/0000-0002-2532-2853>
 Kathryn V. Lester  <https://orcid.org/0000-0002-9903-9911>
 Nicholas Law  <https://orcid.org/0000-0001-9380-6457>
 Andrew W. Mann  <https://orcid.org/0000-0003-3654-1602>
 George R. Ricker  <https://orcid.org/0000-0003-2058-6662>
 Roland K. Vanderspek  <https://orcid.org/0000-0001-6763-6562>
 David W. Latham  <https://orcid.org/0000-0001-9911-7388>
 S. Seager  <https://orcid.org/0000-0002-6892-6948>
 Jon M. Jenkins  <https://orcid.org/0000-0002-4715-9460>
 Joshua N. Winn  <https://orcid.org/0000-0002-4265-047X>
 Douglas A. Caldwell  <https://orcid.org/0000-0003-1963-9616>
 David Charbonneau  <https://orcid.org/0000-0002-9003-484X>
 Christopher J. Burke  <https://orcid.org/0000-0002-7754-9486>
 Zahra Essack  <https://orcid.org/0000-0002-2482-0180>

References

- Agol, E., Luger, R., & Foreman-Mackey, D. 2020, *AJ*, **159**, 123
 Astropy Collaboration, Price-Whelan, A. M., Sipőcz, B. M., et al. 2018, *AJ*, **156**, 123
 Ballard, S. 2019, *AJ*, **157**, 113
 Benedict, G. F., Henry, T. J., Franz, O. G., et al. 2016, *AJ*, **152**, 141
 Boyajian, T. S., von Braun, K., van Belle, G., et al. 2012, *ApJ*, **757**, 112
 Brown, T. M., Baliber, N., Bianco, F. B., et al. 2013, *PASP*, **125**, 1031
 Bryson, S. T., Jenkins, J. M., Gilliland, R. L., et al. 2013, *PASP*, **125**, 889
 Ciardi, D. R., Beichman, C. A., Horch, E. P., & Howell, S. B. 2015, *ApJ*, **805**, 16
 Cloutier, R., & Menou, K. 2020, *AJ*, **159**, 211
 Cloutier, R., Astudillo-Defru, N., Bonfils, X., et al. 2019, *A&A*, **629**, A111
 Collaboration, A., Robitaille, T. P., Tollerud, E. J., et al. 2013, *A&A*, **558**, A33
 Collins, K. 2019, AAS Meeting, **233**, 140.05
 Collins, K. A., Kielkopf, J. F., Stassun, K. G., & Hessman, F. V. 2017, *AJ*, **153**, 77
 Coughlin, J. L., Mullally, F., Thompson, S. E., et al. 2016, *ApJS*, **224**, 12
 Deck, K. M., Agol, E., Holman, M. J., & Nesvorný, D. 2014, *ApJ*, **787**, 132
 Dressing, C. D., & Charbonneau, D. 2015, *ApJ*, **807**, 45
 2019, Exoplanet Follow-up Observing Program - TESS, IPAC, doi:10.26134/EXOPOP3
 Eyley, V. V., Albrecht, S., Huang, X., et al. 2019, *AJ*, **157**, 61
 Fabricius, C., Luri, X., Arenou, F., et al. 2021, *A&A*, **649**, A5
 Fausnaugh, M. 2021, TESS Image Calibrator Full Frame Images ("TICA"), STScI/MAST, doi:10.17909/T9-9J8C-7D30
 Fausnaugh, M. M., Burke, C. J., Ricker, G. R., & Vanderspek, R. 2020, *RNAAS*, **4**, 251
 Foreman-Mackey, D., Luger, R., Agol, E., et al. 2021, *JOSS*, **6**, 3285
 Fulton, B. J., & Petigura, E. A. 2018, *AJ*, **156**, 264
 Fulton, B. J., Petigura, E. A., Howard, A. W., et al. 2017, *AJ*, **154**, 109
 Gaia Collaboration, Vallenari, A., Brown, A. G. A., et al. 2022, arXiv:2208.00211
 Gelman, A., & Rubin, D. B. 1992, *StaSc*, **7**, 457
 Giacalone, S., & Dressing, C. D. 2020, Triceratops: Candidate Exoplanet Rating Tool, Astrophysics Source Code Library, ascl:2002.004
 Gilbert, E. A., Barclay, T., Schlieder, J. E., et al. 2020, *AJ*, **160**, 116
 Guerrero, N. M., Seager, S., Huang, C. X., et al. 2021, *ApJS*, **254**, 39
 Gunther, M. N., Pozuelos, F. J., Dittmann, J. A., et al. 2019, *NatAs*, **3**, 1099
 Harris, C. R., Millman, K. J., van der Walt, S. J., et al. 2020, *Natur*, **585**, 357
 Hartman, J. D., & Bakos, G. Á. 2016, *A&C*, **17**, 1
 Henden, A. A., Templeton, M., Terrell, D., et al. 2016, *yCat*, **II**, 336
 Hoffman, M. D., & Gelman, A. 2011, arXiv:1111.4246
 Howell, S. B., Everett, M. E., Horch, E. P., et al. 2016, *ApJL*, **829**, L2
 Howell, S. B., Everett, M. E., Sherry, W., Horch, E., & Ciardi, D. R. 2011, *AJ*, **142**, 19

- Howell, S. B., Matson, R. A., Ciardi, D. R., et al. 2021, *AJ*, **161**, 164
- Huang, C. X. 2020, TESS Lightcurves From The MIT Quick-Look Pipeline (“QLP”), STScI/MAST, doi:10.17909/T9-R086-E880
- Huang, C. X., Vanderburg, A., Pál, A., et al. 2020a, arXiv:2011.06459 [astro-ph]
- Huang, C. X., Quinn, S. N., Vanderburg, A., et al. 2020b, *ApJL*, **892**, L7
- Hunter, J. D. 2007, *CSE*, **9**, 90
- Jenkins, J. M. 2002, *ApJ*, **575**, 493
- Jenkins, J. M., Tenenbaum, P., Seader, S., et al. 2017, Kepler Science Document KSCI-19081-002, **9**
- Jenkins, J. M., Radziwill, N. M., Bridger, A., et al. 2010, *Proc. SPIE*, **7740**, 77400D
- Jenkins, J. M., Twicken, J. D., McCauliff, S., et al. 2016, *Proc. SPIE*, **9913**, 99133E
- Jensen, E. 2013, Tapir: A Web Interface for Transit/Eclipse Observability, Astrophysics Source Code Library, ascl:1306.007
- Kempton, E. M.-R., Bean, J. L., Louie, D. R., et al. 2018, *PASP*, **130**, 114401
- 2019, Kepler Objects of Interest DR 25 Table, IPAC, doi:10.26133/NEA5
- Kipping, D. M. 2013a, *MNRAS*, **435**, 2152
- Kipping, D. M. 2013b, *MNRAS*, **434**, L51
- Kostov, V. B., Schlieder, J. E., Barclay, T., et al. 2019, *AJ*, **158**, 32
- Kovacs, G., Zucker, S., & Mazeh, T. 2002, *A&A*, **391**, 369
- Kumar, R., Carroll, C., Hartikainen, A., & Martin, O. 2019, *JOSS*, **4**, 1143
- Lester, K. V., Matson, R. A., Howell, S. B., et al. 2021, *AJ*, **162**, 75
- Li, J., Caldwell, D. A., Jenkins, J. M., et al. 2018, AAS Meeting Abstracts, 232, 120.03
- Li, J., Tenenbaum, P., Twicken, J. D., et al. 2019, *PASP*, **131**, 024506
- Lissauer, J. J., Marcy, G. W., Rowe, J. F., et al. 2012, *ApJ*, **750**, 112
- Lithwick, Y., Xie, J., & Wu, Y. 2012, *ApJ*, **761**, 122
- Luger, R., Agol, E., Foreman-Mackey, D., et al. 2019, *AJ*, **157**, 64
- Mann, A. W., Feiden, G. A., Gaidos, E., Boyajian, T., & Braun, K. v. 2015, *ApJ*, **804**, 64
- Matson, R. A., Howell, S. B., Horch, E. P., & Everett, M. E. 2018, *AJ*, **156**, 31
- McCully, C., Volgenau, N. H., Harbeck, D.-R., et al. 2018, *Proc. SPIE*, **10707**, 107070K
- Morris, R. L., Twicken, J. D., Smith, J. C., et al. 2020, Kepler Science Document KSCI-19081-002, **6**
- Morton, T. D., & Johnson, J. A. 2011, *ApJ*, **738**, 170
- Owen, J. E., & Wu, Y. 2013, *ApJ*, **775**, 105
- Paredes, L. A., Henry, T. J., Quinn, S. N., et al. 2021, *AJ*, **162**, 176
- Reback, J., McKinney, W., jbrockmendel, et al. 2020, Pandas-Dev/Pandas: Pandas 1.0.3, Zenodo, doi:10.5281/zenodo.3715232
- Ricker, G. R., Winn, J. N., Vanderspek, R., et al. 2015, *JATIS*, **1**, 014003
- Rodriguez, J. E., Vanderburg, A., Zieba, S., et al. 2020, *AJ*, **160**, 117
- Rogers, L. A. 2015, *ApJ*, **801**, 41
- Salvatier, J., Wiecki, T. V., & Fonnesbeck, C. 2016, *PeerJ Comp. Sci.*, **2**, e55
- Scott, N. J., Howell, S. B., Gnilka, C. L., et al. 2021, *FrASS*, **8**, 138
- Seager, S., & Mullen-Ornelas, G. 2003, *ApJ*, **585**, 1038
- Stassun, K. G., Oelkers, R. J., Pepper, J., et al. 2018, *AJ*, **156**, 102
- Stassun, K. G., Oelkers, R. J., Paegert, M., et al. 2019, *AJ*, **158**, 138
- Team, M. 2021, TESS Target Pixel Files—All Sectors, STScI/MAST, doi:10.17909/T9-YK4W-ZC73
- The Theano Development Team, Al-Rfou, R., Alain, G., et al. 2016, arXiv:1605.02688
- Thompson, S. E., Coughlin, J. L., Hoffman, K., et al. 2018, *ApJS*, **235**, 38
- Tokovinin, A. 2018, *PASP*, **130**, 035002
- Tokovinin, A., Fischer, D. A., Bonati, M., et al. 2013, *PASP*, **125**, 1336
- Twicken, J. D., Radziwill, N. M., Bridger, A., et al. 2010, *Proc. SPIE*, **7740**, 774023
- Twicken, J. D., Catanzarite, J. H., Clarke, B. D., et al. 2018, *PASP*, **130**, 064502
- Van Eylen, V., Astudillo-Defru, N., Bonfils, X., et al. 2021, *MNRAS*, **507**, 2154
- Vanderburg, A., & Johnson, J. A. 2014, *PASP*, **126**, 948
- Vanderburg, A., Huang, C. X., Rodriguez, J. E., et al. 2019, *ApJL*, **881**, L19
- Virtanen, P., Gommers, R., Oliphant, T. E., et al. 2020, *NatMe*, **17**, 261
- Winn, J. N., & Fabrycky, D. C. 2015, *ARA&A*, **53**, 409
- Wolfgang, A., Rogers, L. A., & Ford, E. B. 2016, *ApJ*, **825**, 19
- Zacharias, N., Finch, C. T., Girard, T. M., et al. 2013, *AJ*, **145**, 44
- Ziegler, C., Tokovinin, A., Briceno, C., et al. 2020, *AJ*, **159**, 19